Numerical simulation of K-, N- and O-regime boundary-layer transition at early nonlinear stage

Xian-Yang JIANG[1], Cunbiao LEE*,[1]

*Corresponding author
State Key Laboratory for Turbulence and Complex Systems, College of Engineering, Peking University,
No. 5 Yiheyuan Road Haidian District, Beijing, 100871, P. R. China,
xyjmh@pku.edu.cn, cblee@mech.pku.edu.cn*

DOI: 10.13111/2066-8201.2019.11.3.7

Received: 17 May 2019/ Accepted: 10 July 2019/ Published: September 2019

7th International Workshop on Numerical Modelling in Aerospace Sciences "NMAS 2019"
15-16 May 2019, Bucharest, Romania, (held at INCAS, B-dul Iuliu Maniu 220, sector 6)
Keynote Speakers

Abstract*: Boundary layer transition is usually associated with the amplification and breakdown of three-dimensional waves (3D waves). However, the details of the development of 3D waves in different transition regimes are not well resolved. The present study attempts to examine the transition process at early nonlinear stages of K-, N-, and O-regimes by the solution of nonlinear parabolized stability equations (NPSE). The spatial and temporal variations of streamwise velocity are compared at the one-spike stage. Timelines and material surfaces are presented using Lagrangian tracking method. The development of 3D waves are observed to contribute to the upward lift and downward sweep of flow behaviors, causing inflectional regions in the boundary layer. The evolution of material surfaces reveals that the nonlinear 3D wave manifests as a warped wave front in the near-wall region and as a soliton-like structure at the upper region of the boundary layer. The 3D wave structure is hypothesized as a soliton-like coherent structure. Markedly similar flow behaviors are observed between the regimes, which indicates a similar underlying physical mechanism.*

Key Words: *transition regimes, three-dimensional waves, transition process*

1. INTRODUCTION

Understanding the transition process of wall-bounded shear flow is essential in the control of turbulent production and aerodynamic design. In general, the process of transition can be ideally divided into five stages, i.e. receptivity, linear growth, nonlinear saturation, secondary instability, and breakdown [1]. When free stream turbulence (FST) is low (turbulent intensity less than 1%), a small disturbance will be linearly amplified as Tollmien-Schlichting waves (TS-waves). This process is known as receptivity, which denotes by which a particular disturbances (free-stream disturbances or wall-induced disturbances) will be amplified within the boundary layer [2]. In some circumstances with high FST, TS-waves may be "bypassed". But generally a TS-wave will grow to a point where a nonlinear interaction develops, accompanied by the resonant amplification of three-dimensional waves. This results in inclined high-shear layers forming within the boundary layer in the shape of characteristic Λ-structures (in an aligned or staggered order), which will subsequently break down into turbulence.

So, the linear amplified two-dimensional TS-wave is often the first step towards transition. The TS-wave was first predicted by linear stability analysis, and then was experimentally verified by the pioneering works of [3] in National Bureau of Standards. It was not until the landmark work of [4] that the three-dimensional nature of boundary-layer instability became apparent. They determined that a two-dimensional TS-wave will interact with mean flow, and then rapidly develop into a three-dimensional wave, which finally breaks down to turbulence (named K-regime transition). In the 1960s, detailed transition processes like three-dimensional behavior, mean flow modification, and nonlinear breakdown were also investigated by [5,6] via hot-wire measurements, but it was still far from a unified view of the transition process. Hama and his colleagues employed hydrogen bubble visualization to complement the hot-wire results, and they observed Λ-structures in a transitional boundary layer [7]. They also found that the TS-wave warps three dimensionally during amplification, acquiring a longitudinal vorticity component along its swept-back front. The kinked high-shear layer, which appears as an inflection in vertical hydrogen bubble time-lines (a "kink"), subsequently develops into a hairpin-shaped, discrete vortex. A localized and intensified "warped wave front" (WWF) was considered as the source of the "kink" that appears prior to the formation of a hairpin-shaped vortex. However, the relation between the WWF and the kinked profiles has not been clearly understood. This emphasizes the need to examine the details of the warping process and the development of a WWF prior to the emergence of Λ-vortices.

A number of investigations have shown that hot-wire signals within the kinked region of the high-shear layer record negative spike (mostly in K-regime transition), termed velocity "spikes" [4,5,7,8], which doubled, tripled, etc. downstream.

The multiple spikes appear to be correlated with ring-like vortices at late stage of transition [9]. But in the initial nonlinear stage, there is only one spike in the streamwise velocity trace [10].

Different hypotheses have been made regarding the mechanism responsible for the generation of the kinked structure and the corresponding velocity spikes. The prevailing explanation is the development of a local high-frequency secondary instability of the primary wave [11]. Some argue that the spike is the result of the development of a hairpin vortex or other discrete vortex filament [4,12].

Others state that the shear turbulence originates from non-hairpin framework, e.g. vorticity wave packet or twisted contact structures [13-15], soliton-like coherent structure [16, 17], spatio-temporal wave front [18]. The soliton-like coherent structure (SCS) was proposed to explain the velocity profile "kink" and the one-spike structure, which is a three-dimensional wavelike structure within the whole boundary layer, covering the near-wall region to the outer edge [19, 20].

This 3D structure was later verified by direct numerical simulation [21] and tomographic particle image velocimetry [22]. However, the role of this 3D wave amplification in early stage boundary layer transition has not previously been examined in detail especially for different transition regimes.

In the present study, three transition regimes are considered: (1) K-regime transition with fundamental resonance of five-wave interaction (namely $(\omega, 0)$, $(\omega, \pm\beta)$, and $(0, \pm\beta)$) [4,8]; (2) N-regime transition with subharmonic resonance between modes $(2\omega, 0)$ and $(\omega, \pm\beta)$ [23, 24]. (3) O-regime transition with oblique breakdown induced by the interaction of a pair of oblique waves $(\omega, \pm\beta)$ [25, 26]. The objective of this numerical study is to examine the detail of the warping process during the transition of one-spike stage and to acquire insight into the role of a 3D wave structure in the transition from a structure-based view by Lagrangian particle tracking method.

2. NUMERICAL METHOD

Parabolized stability equation (PSE) are useful in the analysis of the streamwise growth of linear and nonlinear disturbances in boundary layer. The use of the PSE approach for transition analysis is one of its most important application. The nonlinear PSE (NPSE) is described in detail in [27], here only a brief introduction is given. The NPSE formulation follows

$$\Psi(x,y,\phi,t) = \bar{\Psi}(x,y) + \sum_{m,n} \hat{\Psi}_{mn}(x,y)\exp\left(i\int_0^x \alpha_{mn}\mathrm{d}x - i\omega_m t + in\phi\right), \tag{1}$$

where $\Psi \equiv (u,v,w,p)$; $\bar{\Psi}$ denotes the basic stage and $\hat{\Psi}_{mn}$ indicates the shape function for the Fourier mode (m, n), the α_{mn} and ω_m are streamwise wavenumber and frequency. The coordinate was normalized using the fixed characteristic thickness $\delta_0 = \left(\frac{\nu\tilde{x}_0}{U_\infty}\right)^{\frac{1}{2}}$, where $\tilde{x}$ is the location where disturbances were introduced. The equation (1) was substituted into the Navier-Stokes equation to yield the governing equation for the shape functions of each mode (m, n) as

$$(\mathcal{L}_0 + \mathcal{L}_1)\hat{\Psi}_{mn} + \frac{\mathcal{L}_2\partial\hat{\Psi}_{mn}}{\partial x} + \frac{\mathrm{d}\alpha_{mn}}{\mathrm{d}x} + \frac{\mathrm{d}\alpha_{mn}}{\mathrm{d}x}\,\mathcal{L}_3\hat{\Psi}_{mn} = \mathcal{F}_{mn}, \tag{2}$$

where $\mathcal{L}_0$ contains the linear –parallel terms, $\mathcal{L}_1$ contains the non-parallel mean-flow terms, $\mathcal{L}_2$ and $\mathcal{L}_3$ arise from the non-parallel disturbance terms, and $\mathcal{L}_{\mathrm{mn}}$ is the nonlinear forcing term. The PSE solution employed no-slip wall condition and vanishing velocity disturbance far-field condition as

$$\hat{u}_{mn}, \hat{v}_{mn}, \hat{w}_{mn} = 0 \text{ at } y = 0 \text{ and } \infty, \tag{3}$$

and the initial condition are provided by the results of the linear stability theory [28]. Equation (2) was marched forward using the Euler backward scheme.

Table 1 gives the parameters of the introduced disturbances for the three transition regimes. The frequency (F) of the 2D TS-wave for K- and N-regimes is 106×10^{-6}, with the amplitude (A) setting as 0.4% of the freestream velocity (U_∞). A pair of oblique waves with amplitude of $0.05\%U_\infty$ was also introduced at x_0. The frequency is 106×10^{-6} and 53×10^{-6} for the K- and N-regime respectively. For O-regime transition, only a pair of oblique waves with the same streamwise frequency and spanwise wavenumber as the K-regime was introduced, but the amplitude of which was set as $0.4\%U_\infty$.

Table 1 Numerical setting for the three transition regimes

Transition regimes	2D TS-wave (ω, A)	3D waves (ω, A, β)
K	(106, $0.4\%U_\infty$)	(106, $0.05\%U_\infty$, 0.05)
N	(106, $0.4\%U_\infty$)	(53, $0.05\%U_\infty$, 0.05)
O	-	(106, $0.4\%U_\infty$, 0.05)

In the following section, the primary TS-wave in K- and N-regime are represented by (1,0), the introduced oblique waves in K- and O-regime are named as (1,±1), and the introduced oblique waves in N-regime denotes (1/2,±1).

3. RESULTS

The contours of streamwise velocity in the *x*-*z* plane at y = 2.5 is shown in Figure 1(*a*-*c*) for the transition of the K-regime, O-regime and N-regime respectively. As shown in Figure 1(a),

the K-regime is characterized by aligned low-momentum zones (LMZs), which appear as the blue downstream regions (see color key). These regions have a spanwise spacing of λ_{z0}=125.6, which is the same as the spanwise wavelength of the corresponding oblique waves. However, for O-regime and N-region, the LMZs both appear as a staggered pattern. The staggered LMZs for the O-regime develop nonlinearly from a pair of oblique waves (1,±1), farther upstream than for the N-regime, with a spanwise wavelength of λ_{z0}=125.6. But the streaks shown in the O-regime is spaced by λz = 1/2 λ_{z0}. This implies the appearance of streak mode (0,2). In both the K-regime and O-regime, the low-speed streak (LSS) consists of several LMZs. The LMZs at far downstream locations for all regimes are flanked by a pair of high-speed regions, which indicate the appearance of Λ-vortices. The LMZ is formed by the lift-up of a 3D wave at the early stage, which appears prior than Λ-vortex, as indicated by the position of LMZs in the figures. It may speculate that Λ-vortex is produced by the nonlinear 3D wave.

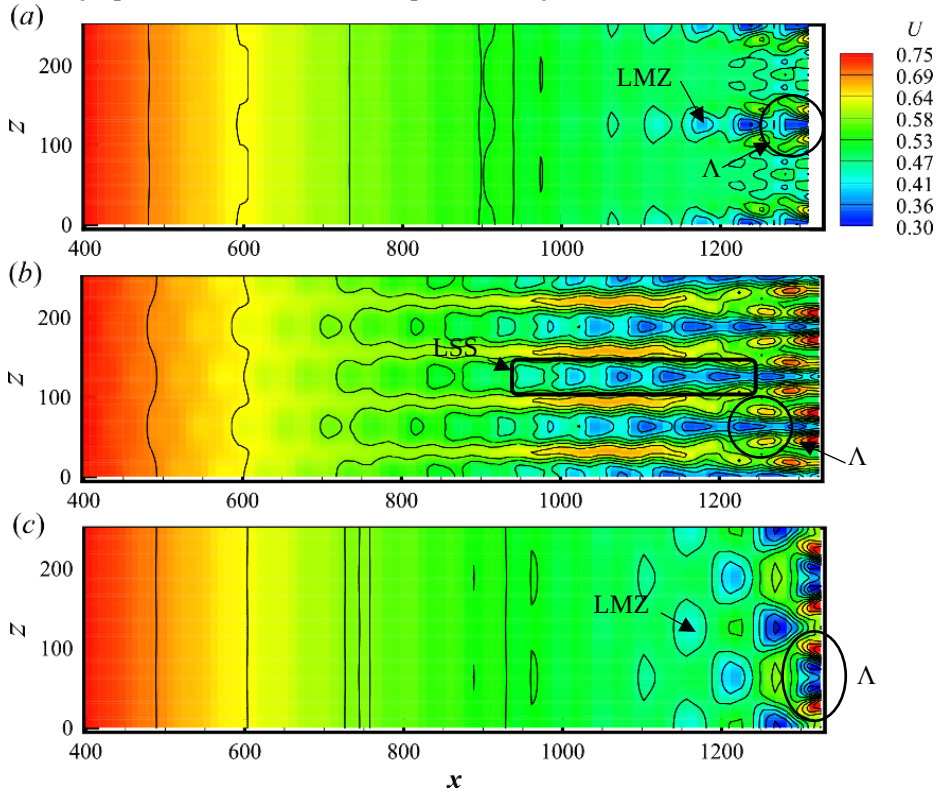

Figure 1. Contour of streamwise velocity U at $y = 2.5$ and $t = 0.8$ T. (*a*) K-regime transition; (*b*) O-regime transition; (*c*) N-regime transition

The spanwise variations of streamwise velocity U at different wall-normal heights for the three cases are illustrated in Figure 2. The streamwise velocity is determined at x = 1296, spanning from z = 0 ~ 250, which encompasses two spanwise 3D wavelength for the respective regimes. Figure 2 shows that the velocity patterns vary strongly with distance from the wall, with the most vigorous variations occurring near the central portion of the boundary layer. In Figure 2(a), a spike-like velocity profile (labelled P1 in the figure) is observed at the position of z = 125.6. Compared to Figure 1, this position is characterized as low-speed streaks (LSS) or LMZs. In Figure 2(b), a second spike labeled P2, is observed at two sides of the P1, representing a second LSS. The phenomenon of spikes in z-distribution of streamwise velocity becomes most apparent at upper portion of the boundary layer, with the amplitude of the

second LSS being sometimes even greater than the primary LSS. Figure 2(c) shows the transverse variation of U for the N-regime. In contrast to the K- and O-regime, the amplitude variation is less, with no apparent spike-like LSS development during this weak nonlinear stage, which is consistent with Figure 1(c). For all the regimes, the velocity distribution appears differently at the upper portion and the near-wall portion of the boundary layer.

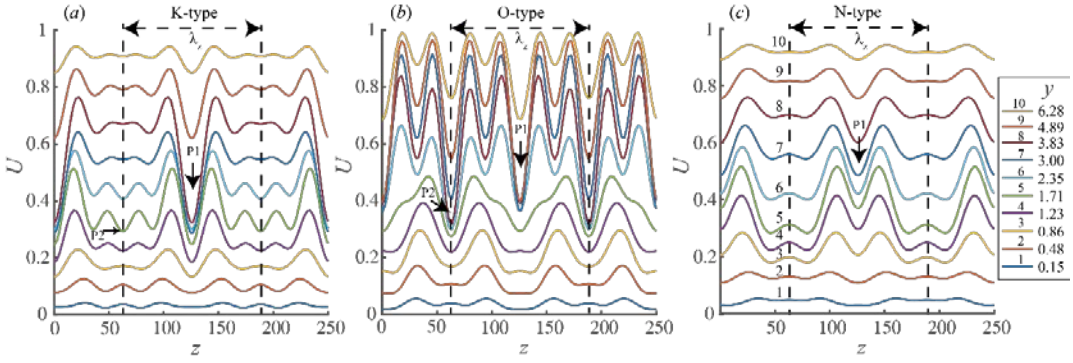

Figure 2. Spanwise variation of streamwise velocity at x = 1296 and t = 0.78 T, with different y. (a) K-regime transition; (b) O-regime transition; (c) N-regime transition

Timeseries of the variations in streamwise velocity U at selected wall-normal positions are shown in Figure 3 for the three transition regimes. The timeseries clearly shows the one-spike stage of transition, since multi-spikes in a period of streamwise velocity trace have not arisen yet for all regimes. Figure 3 shows that a phase shift (marked by dashed lines) develops with distance from the wall. The waveform of U in the central portion of boundary layer deforms from sinusoidal shape into an asymmetric one, appearing as bottle shape with a plateau (marked by arrows). This is most apparent for the O-regime transition, as shown in Figure 3(b). The plateau in the velocity timeseries may be due to the appearance of higher frequency modes nonlinearly developed from the interaction of the oblique waves.

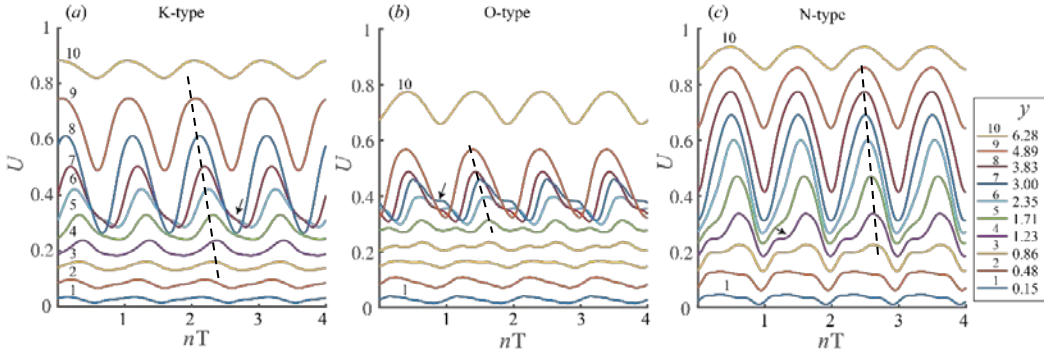

Figure 3. Time series of streamwise velocity at x = 1296, with different y. (a) K-regime transition; (b) O- regime transition; (c) N-regime transition

Several classical experimental and numerical visualization of marked particles provided time-line patterns of boundary layer transition, e.g. [7, 10, 29, 30]. A similar visualization of marked particles as [30, 31] is implemented by the integration of

$$\frac{\partial \xi}{\partial \tau} = v(\xi_1 - c_{TS}\tau, \xi_2, \xi_3; t) \quad (\xi(0) = \xi_0), \tag{4}$$

where $\xi(0)$ is the initial position of the marked particle at t =0, $\xi(t)$ is the position of a particle in the rest frame, and $v(x,t)$ denotes the velocity field in the rest frame. Figure 4

shows the timeline surface of the three transition regimes at t = 2.7T, initiated at x = 795, y=1.71. Here T indicates Tollmien-Schlichting period. The contour in the figure indicates the wall-normal distance. For K-regime transition, the 2D timelines progressively develop into 3D timelines with the wave front warped, as shown in Figure 4(*a*). We term the warped wave front as WWF, which is a manifestation of the developed three-dimensional wave structure in timeline sheet. At a downstream position, the WWF lifts up and develops into a Λ-vortex. The warping process of timelines sheet occurs similarly for the O- and N-regime transition, as shown in Figure 4(*b*) and (*c*). The spanwise stripe for N-regime transition have a slight waviness in the spanwise direction initially (WWF), and becomes a folded particle sheet downstream, which eventually becomes screw-like structure of the Λ-legs. But there is no spanwise WWF for the O-regime, where the WWF is staggered initially and develops into Λ-vortex earlier than the other two regimes. When compared with the velocity contours shown in Figure 1, the pattern of the WWF looks markedly similar to the pattern of LMZ. Thus, it may further hypothesize that the low-speed streak consists of WWFs.

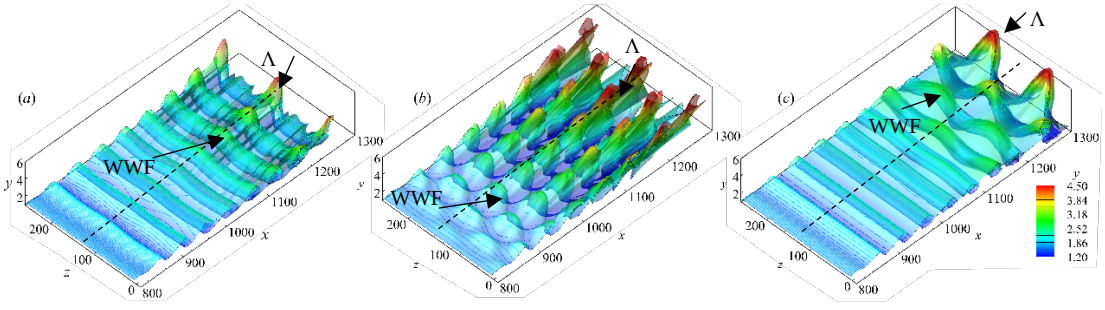

Figure 4. Time-line surfaces for K-regime transition (a), O-regime transition (b) and N-regime transition (c) at t = 2.7T, initiated at x = 795, y=1.71

Figure 5 shows the timelines starting from a wire in the middle plane (*x*-*y* plane in the dashed line of Figure 4) at t = 3.4T for the three transition regimes, simulating visualizations with a bubble wire normal to the wall at peak position. The K-regime transition shows that the inflectional region (labeled 1) progressively develops into warp wave front (labeled 2-4). The lift-up of a WWF induces an upward motion (labeled E) and downward motion (labeled S). The strongly distortion of the timelines indicates the position of high-shear layer. Similar patterns of timelines for O- and N-regimes are shown in Figure 5(*b*) and (*c*). The WWF appears at a higher position for O-regime than for N-regime, and the latter of which develops in near-wall region initially. The roll-up behavior is not apparent at the time t =3.4T, indicating that a discrete vortex has not developed yet. The pattern shown in Figure 5 is markedly similar to the hydrogen bubble visualization of [7], who term the initial inflectional region as a "kink" structure.

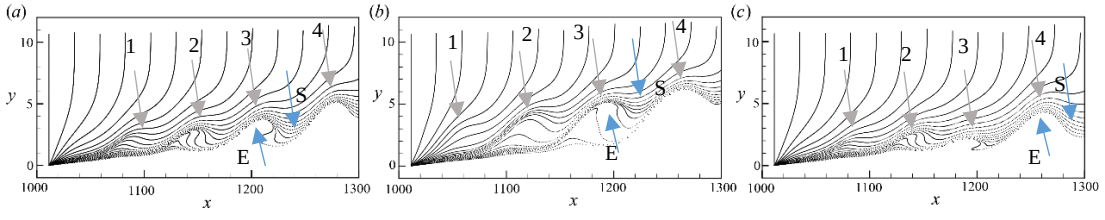

Figure 5. Side views of vertical time-lines at t = 3.4T, (a) K-regime; (b) O-regime; (c) N-regime.

Figure 6 shows the deformation of two material surfaces at selected wall-normal positions, i.e. y= 1.71 and 5.89, at t = 2T. The traced particles of which are initially in a flat surface. The

contour in the figure indicates the wall-normal position, see the color key on the right. For the K-regime transition, the surface in the near-wall region represents a similar warped structure of Figure 4. While the surface at the upper portion of the boundary layer shows the development of 2D wave into 3D wave with no apparent warping. The deformation of material surfaces for N-regime is quite similar to K-regime, but they undergoes a stronger warping process with higher amplitude of the 3D wave, as shown in Figure 6(*c*). For the O-regime transition, it clearly shows the appearance of 3D wave in the region of LSS at the upper surface. In Figure 6, the white lines in the middle of the surface indicate the profile of the deformed surface. The side view of these profiles at more selected wall-normal positions are shown in Figure 7 at the same time of Figure 6.

-

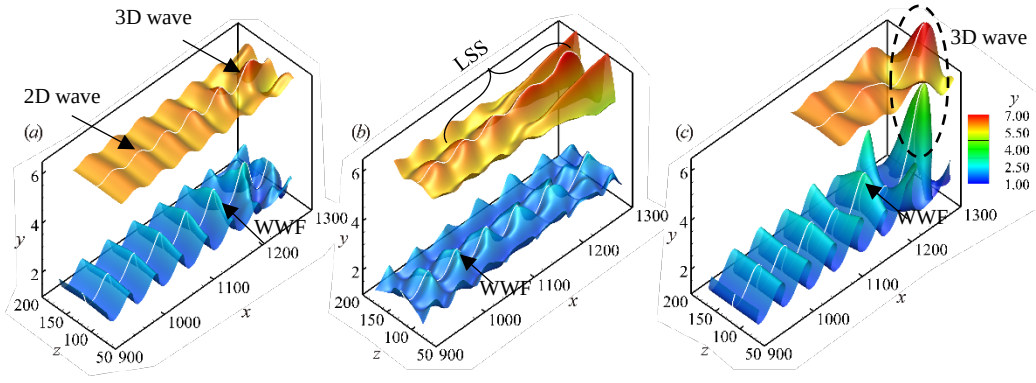

Figure 6. Deformation of material surfaces at t = 2T, initiated at y = 1.71 and 5.89: (a) K-regime; (b) O-regime; (c) N-regime

Figure 7(*a*) clearly shows that the most vigorous warping process occurs in the near-wall region, and the warped wave front tends to roll up at a downstream position. But the surface profiles at the upper boundary layer undulate periodically, growing the amplitude of their waveform. For the O-regime, the warped wave front appears at higher positions (labeled 3 and 4). The surface profiles at the near-wall region (e.g. 1 and 2) represent a spike-like pattern, indicated as A in Figure 7(*b*), which protrudes upward to lift the boundary layer away from the wall. This introduces a strong inflectional region of vertical timelines in Figure 5(*b*). In contrast, the surface profiles further from the wall (e.g. 6 to 11) indicate only minimal amplification, with an inclination away from the surface as they advent downstream. For the N-regime, the near-wall surface profiles are strongly warped, with their amplitude amplifying rapidly at the position of $x \approx 1250$. The wavelength of this amplified 3D wave is nearly twice that of the initial TS- wave. This strong amplification is hypothesized to be due to subharmonic resonance of N-regime transition. Note that prior to the amplification of a 3D wave, there appears to be a relatively quiet zone, labeled E in Figure 7(*c*), which is similar to the wave breakdown behavior within a compressible boundary layer (Li et al. 2010; Zhang et al. 2013). The presence of this quiet zone before the development of the amplified 3D wave is also reflected in the timeline patterns shown in Figure 5(*c*). The presence of this quiet zone is hypothesized to be the result of a nonlinear interaction between waves, i.e. the attenuation of the primary wave and the growth of a low-frequency disturbance. The mechanism of development of this quiet zone merits further study. An additional significant observation is that the surface profiles for all the regimes at the central portion of the boundary layer (e.g. 3 and 4) display a significant secondary peak that is superposed on the primary wave, denoted

as C in the figure. This strong secondary peak appears to be correlated with the folding behavior of the particle surface. For all the transition regimes, the structures at the upper boundary layer are similar to solitary waves propagating downstream with little dissipation. However, both the soliton-like wave structures at the upper region or the warped wave front at the near-wall region are essentially caused by the same structure, which is hypothesized as a soliton-like coherent structure (SCS).

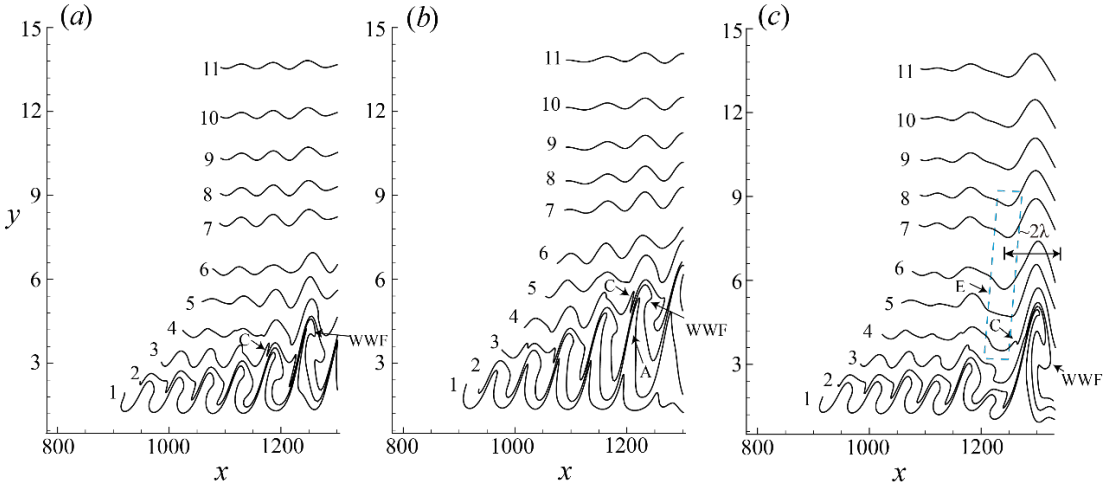

Figure 7. Material lines corresponds to the profile at the middle plane of the deformed surface in Figure 6 at t = 2T, (a) K-regime; (b) O-regime; (c) N-regime. The number labeled 1,2,...,11 correspond to wall-normal position y = 1.71, 2.35, 3.00, 3.83, 4.89, 5.89, 7.61, 8.68, 9.94,11.42, 13.17.

4. SUMMARY AND CONCLUSIONS

In this paper, nonlinear parabolized stability equation (NPSE) is solved numerically to simulate the transition of K-, O- and N-regimes at early nonlinear stage. The contours of instantaneous streamwise velocity for the three regimes are displayed in a *x*-*z* plane, which reveal the classical aligned or staggered pattern of low momentum zone (LMZ). The presence of the LMZ is due to the appearance of three-dimensional wave (3D wave) that is produced nonlinearly by the amplified disturbances. The low-speed streak (LSS) for K- and O- regime transition is observed to consist of several LMZs. The time series of streamwise velocity shows the one-spike stage of the regimes, which illustrates the phase shift and the deformation of waveform developing with distance from the wall. Numerical visualization is reconstructed based on the Lagrangian tracking of marked particles to compare with previous experimental results. The timelines sheet at the near-wall region for all transition regimes represents a warped wave front (WWF) which eventually develops into a Λ-vortex downstream. The timeline profiles in the vertical plane further provide the detail of warping process, which reveal the upward and downward motions caused by the lift-up of the WWF. The deformation of traced material surfaces for the three regimes display 3D wave structures at different wall-normal positions, indicating that the WWF is caused by the amplification of the 3D wave. The warping and amplifying processes are finally shown by the surface profiles initiated at different wall-normal positions in the middle plane. The nonlinear 3D wave manifests as a warped wave front in the near-wall region and as a soliton-like wave structure at the upper region of the boundary layer. The 3D wave structure is further hypothesized as a soliton-like coherent structure.

ACKNOWLEDGEMENTS

This research was supported by the National Natural Science Foundation of China (10921202, 11221061, 11632002, 11521091 and 11602005). The authors are thankful to Professor C. R. Smith for his valuable comments on this work. Furthermore, the authors gratefully acknowledge the support of Dr. X. Chen for the PSE approach.

REFERENCES

[1] P. J. Schmid & D. S. Henningson, *Stability and transition in shear flows*, New York: Springer-Verlag, 2001.
[2] E. Reshotko, Boundary-layer stability and transition, *Annual Review of Fluid Mechanics*, **8** (1), 311–349, 1976.
[3] G. B. Schubauer & H. K. Skramstad, *Laminar-boundary-layer oscillations and transition on a flat plate*, Tech. Rep., National Aeronautics and Space Administration Washington DC, 1943.
[4] P. S. Klebanoff, K. D. Tidstrom & L. M. Sargent, The three-dimensional nature of boundary-layer instability, *Journal of Fluid Mechanics* **12** (1), 1-34, 1962.
[5] L. S. G. Kovasznay, H. Komoda & B. R. D Vasudeva, *Project SQUID: Detailed flow field in transition*, Defense Technical Information Center, 1962.
[6] I. Tani, Boundary-layer transition, *Annual Review of Fluid Mechanics* **1** (1), 169–196, 1969.
[7] F. R. Hama & J. Nutant, *Detailed flow-field observations in the transition process in a thick boundary layer*, In Proceedings of the Heat Transfer and Fluid Mechanics Institute, 16, 77–93, Stanford University Press, 1963.
[8] Y. S. Kachanov, Physical mechanisms of laminar-boundary-layer transition, *Annual Review of Fluid Mechanics* **26** (1), 411–482, 1994.
[9] V. I. Borodulin, V. R. Gaponenko, Y. S. Kachanov, D. G. W. Meyer, U. Rist, Q. X. Lian & C. B. Lee, Late-stage transitional boundary-layer structures. Direct numerical simulation and experiment, *Theoretical and Computational Fluid Dynamics* **15** (5), 317–337, 2002.
[10] E. Laurien & L. Kleiser, Numerical simulation of boundary-layer transition and transition control, *Journal of Fluid Mechanics*, **199**, 403-440, 1989.
[11] A. Nayfeh, Nonlinear stability of boundary layers, *AIAA paper, No. 87-0044*, 1987.
[12] D. Rempfer & H. F. Fasel, Evolution of three-dimensional coherent structures in a flat-plate boundary layer, *Journal of Fluid Mechanics* **260**, 351-375, 1994.
[13] H. Dumitrescu & V. Cardos, The origin of shear turbulence, *INCAS BULLETIN*, vol **9**, iss 4, (online) ISSN 2247–4528, (print) ISSN 2066–8201, ISSN–L 2066–8201, DOI: 10.13111/2066-8201.2017.9.4.7, 75-89, 2017.
[14] H. Dumitrescu, V. Cardos & R. Bogateanu, Random turbulence versus structured turbulence, *INCAS BULLETIN*, vol 10, iss 4, (online) ISSN 2247–4528, (print) ISSN 2066–8201, ISSN–L 2066–8201, DOI: 10.13111/2066-8201.2018.10.4.5, 45-60, 2018.
[15] H. Dumitrescu, V. Cardos & R. Bogateanu, Twisted Contact Structures in Turbulent Flows, *INCAS BULLETIN*, vol 11, iss 1, (online) ISSN 2247–4528, (print) ISSN 2066–8201, ISSN–L 2066–8201, DOI: 10.13111/2066-8201.2019.11.1.7, 91-106, 2019.
[16] C. B. Lee & R. Q. Li, Dominant structure for turbulent production in a transitional boundary layer, *Journal of Turbulence* **8** (55), 1–34, 2007.
[17] C. B. Lee & J. Z. Wu, Transition in wall-bounded flows, *Applied Mechanics Reviews* **61**, 030802, 2008.
[18] S. Bhaumik & T. K. Sengupta, Precursor of transition to turbulence: spatiotemporal wave front, *Physics Review E* **89** (4), 043018, 2014.
[19] C. B. Lee, New features of CS solitons and the formation of vortices, *Physics Letters A* **247** (6), 397–402, 1998.
[20] C. B. Lee, Possible universal transitional scenario in a flat plate boundary layer: Measurement and visualization, *Physical Review E* **62** (3), 3659–3670, 2000.
[21] W. Chen, *Numerical simulation of boundary layer transition by combined compact difference method*, PhD thesis, Nanyang Technological University, Nanyang Ave, Singapore, 2013.
[22] X. Y. Jiang, Revisiting coherent structures in low-speed turbulent boundary layers. *Applied Mathematics and Mechanics (English Edition)* **40** (2), 261–272, 2019a.
[23] Y. S. Kachanov & V. Y. Levchenko, The resonant interaction of disturbances at laminar turbulent transition in a boundary-layer, *Journal of Fluid Mechanics* **138**, 209–247, 1984.
[24] T. Herbert, Analysis of the subharmonic route to transition in boundary layers, *AIAA Paper No. 84-0009*, 1984.
[25] M. E. Goldstein & S.-W. Choi, Nonlinear evolution of interacting oblique waves on two-dimensional shear layers, *Journal of Fluid Mechanics* **207**, 97–120, 1989.

[26] P. Schmid, & D. Henningson, A new mechanism for rapid transition involving a pair of oblique waves, *Physics of Fluids* **4** (9), 1986–1989, 1992.
[27] F. P. Bertolotti, T. Herbert & P. R. Spalart, Linear and nonlinear stability of the blasius boundary-layer. *Journal of Fluid Mechanics* **242**, 441–474, 1992.
[28] X. Chen, Y. D. Zhu & C. B. Lee, Interactions between second mode and low-frequency waves in a hypersonic boundary layer, *Journal of Fluid Mechanics* **820**, 693–735, 2017.
[29] F. X. Wortmann, *Boundary-layer waves and transition*. In Advances in Fluid Mechanics, E. Krause (Eds.), pp. 268–279. Berlin, Heidelberg: Springer, 1981.
[30] W. S. Saric, Visualization of Different Transition Mechanisms, *Physics of Fluids*, **29**, 2770, 1986.
[31] X. Y. Jiang, Lagrangian identification of coherent structures in wall-bounded flows, *Advance Applied Mathematics and Mechanics* **11**, 640–652, 2019b.